

Optical Engineering

SPIDigitalLibrary.org/oe

Large-aperture approximation for not-so-large apertures

Chris Porter
Stanislav Gordeyev
Eric Jumper



Large-aperture approximation for not-so-large apertures

Chris Porter
USAF Academy
Department of Aeronautics
Colorado 80840

Stanislav Gordeyev
Eric Jumper
University of Notre Dame
Department of Mechanical and Aerospace
Engineering
Hessert Laboratory for Aerospace Research
Notre Dame, Indiana 46556
E-mail: sgordeye@nd.edu

Abstract. In-flight wavefront measurements around a flat-window turret at subsonic Mach numbers are analyzed in instantaneous and time-averaged sense. In addition to the root-mean-squared levels of aero-optical distortions, higher-order spatial statistics are calculated, and their dependence as a function of the viewing angle is discussed. Given the optical data obtained, the applicability of the commonly used large aperture approximation (LAA) is revisited. We show that, for all angles, the LAA consistently underestimates the time-averaged Strehl ratio, so the LAA should be used very cautiously. Some reasons for these discrepancies are traced to non-Gaussian spatial distribution of the optical wavefronts. A different approximation for computing time-averaged Strehl ratios is proposed, and the results are discussed. © 2013 Society of Photo-Optical Instrumentation Engineers (SPIE) [DOI: [10.1117/1.OE.52.7.071417](https://doi.org/10.1117/1.OE.52.7.071417)]

Subject terms: Fourier optics; laser applications; optical systems; turbulence; wavefronts.

Paper 121457SS received Oct. 5, 2012; revised manuscript received Feb. 22, 2013; accepted for publication Feb. 25, 2013; published online Mar. 14, 2013.

1 Introduction

In the last decade, the introduction of more powerful lasers with a shorter wavelength (1 to 1.5 μm) provided a new impulse for developing airborne laser-based systems for both direct-energy deposition and communication purposes. However, the shorter wavelengths increased the detrimental effects of inhomogeneous refractive mediums¹⁻³ on the ability of optical systems to focus a laser beam in the far field.

From an optical point of view, hemisphere-on-cylinder turrets appear to offer the maximum field of regard, and from a design point of view, they provide a simple and efficient means to project or receive a laser beam.⁴ However, the complex flow around a turret at high subsonic and transonic speeds creates pressure and temperature fluctuations, which result in density fluctuations. Because the index of refraction in air is directly related to density through the Gladstone-Dale constant, K_{GD} , $n(x, t) - 1 = K_{\text{GD}}\rho(x, t)$, these density fluctuations result in index-of-refraction fluctuations. The index-of-refraction variations in compressible flows, referred to as aero-optical effects,⁵ impose aberrations on the outgoing laser beam that reduce the peak irradiance of the laser beam in the far field and can severely limit an airborne directed-energy system's field of regard. The aberrations with correlation lengths larger than the aperture primarily cause the beam to tip and tilt. This can be corrected with an appropriate-bandwidth fast steering mirror. However, aero-optical aberrations that are smaller than the aperture impose higher-order aberrations that scatter the beam, reducing the beam's peak intensity in the far field. From a systems point of view, the so-called large aperture approximation is a handy way of estimating the reduction in intensity from that achievable with an unaberrated diffraction-limited beam. This paper revisits the accuracy of the large aperture approximation by looking at the statistics of wavefronts collected in flight from the Airborne Aero-Optics Laboratory⁶ (AAOL).

Aberrations are imposed on the beam as some parts of the wavefront travel faster over a given time period than other wavefront parts. To quantify the level of aero-optical distortions, the optical path difference (OPD) is calculated as $\text{OPD}(x, y, t) = \text{OPL}(x, y, t) - \langle \text{OPL}(x, y, t) \rangle$, where the optical path length (OPL), is defined as $\text{OPL}(x, y, t) = \int_{z_1}^{z_2} n(x, y, z, t) dz$, and the angle brackets represent the spatially averaged optical path length over the aperture at a given time t . The system of coordinate is chosen as such that the z -axis is aligned with the beam direction.

Usually, to characterize the effect that changes in OPD across the aperture have on the far field, the instantaneous Strehl ratio SR is determined. However, it is common practice to remove tip/tilt first, so that only the effects of the higher-order aberrations (i.e., beam scatter/spread) are examined. The Strehl ratio is defined as a ratio of the on-axis irradiance I to the diffraction-limited on-axis irradiance I_0 . In general, for wavefronts with a uniform intensity distribution, and assuming that the target is at or near the laser beam focal plane, which is almost always the case, the Fraunhofer approximation is used⁷ to provide accurate Strehl ratio results. Thus,

$$\text{SR}(t) = \frac{\left| \iint \exp\left[i \frac{2\pi}{\lambda} \text{OPD}(x, y, t)\right] dx dy \right|^2}{\left(\iint dx dy \right)^2}. \quad (1)$$

If the spatial probability distribution of $\text{OPD}(x, y, t)$ is Gaussian at a given moment t , then the exponential form of the Maréchal approximation¹ accurately predicts the instantaneous Strehl ratio; that is,

$$\text{SR}(t) = \frac{I}{I_0} = \exp\left(-\left[\frac{2\pi \text{OPD}_{\text{rms}}(t)}{\lambda}\right]^2\right), \quad (2)$$

where OPD_{RMS} is the spatial root mean square of the OPD over the aperture, and λ is the wavelength of the laser. It should be emphasized that, as long as the spatial wavefront statistics is Gaussian, Eq. (2) remains accurate regardless of

the amplitude of OPD_{RMS} . Steinmetz⁸ showed that, in the limit when the aperture size is much larger than the characteristic turbulence structure size, the Maréchal approximation is approximately valid for any statistical processes, and that the *time-averaged* Strehl ratio, if the time-averaged OPD_{RMS} is used, is

$$\overline{SR} = \exp\left(-\left[\frac{2\pi\overline{OPD}_{rms}}{\lambda}\right]^2\right). \quad (3)$$

This approximation is called the large-aperture approximation and is widely used to estimate far-field effects on a target. However, it is usually accompanied by the caveat that the approximation is only valid up to amplitudes¹ of approximately 0.1λ . In that which follows, time-resolved in-flight wavefront data from the hemisphere-cylinder AAOL turret in a flat-window configuration in fully subsonic flow over the turret⁹ is analyzed to assess the accuracy of Eqs. (2) and (3), with special attention paid to the wavefront statistics.

2 AAOL Wavefront Analysis

Series of time- and space-resolved wavefronts were collected with a high-speed Shack-Hartmann sensor⁶ on board the AAOL. The AAOL is described by Jumper et al.,⁶ and details of wavefront measurements and other relevant experimental information are described by Porter et al.⁹ and De Lucca et al.¹⁰ The AAOL flight program consists of two citations flying in formation approximately 50 m apart to minimize atmospheric effects. A slowly diverging continuous YAG:Nd 5-Watt laser beam with $\lambda = 532$ nm approximately 3 mm in diameter was sent from a chase plane to an airborne laboratory. The flight-test airborne laboratory consists of a turret 30.5-cm (one-foot) in diameter with a 10.2-cm (four-inch) flat-window clear aperture, as shown in Fig. 1(a). At 50 m, the beam from the chase aircraft is diverged to approximately 20 cm, so that it overfills the turret clear aperture by a factor of two; once the laser and turret systems are tracking each other, a 2.0-cm stabilized beam emerges from the turret mount on to an optical bench in the laboratory aircraft. The spherical figure of the beam

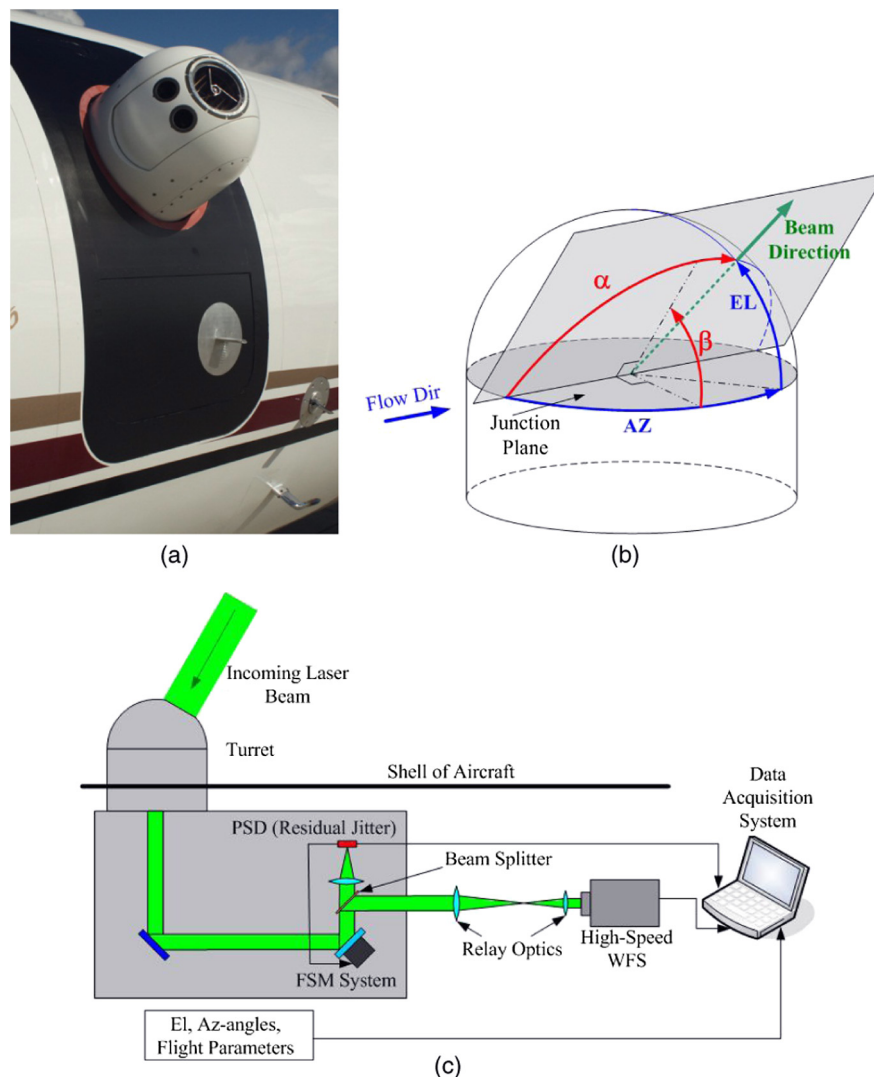


Fig. 1 (a) The AAOL turret with a flat window. (b) Definition of angles to describe the beam direction. (c) Optical setup of the beam path and suite of instruments during flight tests.

due to the divergence from the chase aircraft is removed from the otherwise aero-optically aberrated beam. The “stabilization” of the beam is performed by a closed-loop fast-steering mirror system that reimaging the turret pupil and can reduce the beam’s overall jitter to a cutoff frequency of approximately 200 Hz. The “stabilized beam” is then split to the various sensors on the optical bench on board the laboratory aircraft, including a high-speed Shack-Hartmann wavefront sensor, as shown in Fig. 1(c).

Although AAOL data were taken at a range of Mach numbers and altitudes, the data analyzed here are for a Mach number of 0.5 at an altitude of 15,000 ft. The spatial resolution of wavefronts was 32×32 . Wavefronts were sampled at a frame rate of either 20 kHz for time-resolved measurements at a fixed azimuth/elevation angle or 3 kHz for collecting OPD statistics over a range of angles. To minimize spatial smearing, the camera’s shutter/integration time was set at $0.5 \mu\text{s}$. During the processing of the wavefronts, steady-lensing aberrations, instantaneous piston, and tip/tilt components were removed from each wavefront, leaving only higher-order aberrations. Finally, the wavefronts $\text{OPD}(x, y, t)$ were normalized^{1,4} as

$$\text{OPD}^{\text{NORM}}(x, y, t) = \frac{\text{OPD}(x, y, t)}{(\rho/\rho_{\text{SL}})M^2D} [\mu\text{m}/\text{m}], \quad (4)$$

where ρ is the freestream density, M is the Mach number, ρ_{SL} is the sea-level density ($\rho_{\text{SL}} = 1.225 \text{ kg}/\text{m}^3$), and D is the turret diameter. For different elevation (EL) and azimuthal

(AZ) angles, we computed time-series of normalized spatial root-mean-square; that is,

$$\begin{aligned} \text{OPD}_{\text{RMS}}^{\text{NORM}}(t) &= \sqrt{\langle (\text{OPD}^{\text{NORM}}(x, y, t))^2 \rangle} \\ &\equiv \frac{\text{OPD}_{\text{RMS}}}{(\rho/\rho_{\text{SL}})M^2D} [\mu\text{m}/\text{m}], \end{aligned}$$

where angle brackets denote spatial averaging [see Fig. 1(b)].

From a flow-physics point of view, it is more convenient to introduce a different coordinate system to describe the beam direction. This coordinate system uses the viewing angle α and the modified elevation angle β to define the direction of the beam, as shown in Fig. 1(b). The viewing angle is defined as the angle between the flow direction and beam direction vectors. The modified elevation angle is defined as the angle between the junction plane joining the hemisphere to the cylinder and the plane formed by the flow direction and beam direction vectors. These angles are related to the azimuth and the elevation angles: $\alpha = \cos^{-1}[\cos(\text{AZ})\cos(\text{EL})]$, and $\beta = \tan^{-1}[\tan(\text{EL})/\sin(\text{AZ})]$.

A summary of the time-averaged aero-optical data for different viewing angles is shown in Fig. 2. In addition, examples of instantaneous wavefronts across the aperture are shown for selected viewing angles of $\alpha = 81, 92, 99,$ and 117 deg. The flow across the aperture goes from left to right. For the viewing angle of 81 deg, the size of the aberrations, relative to the aperture, were smaller and less coherent than the structures seen at the backward-looking angles.

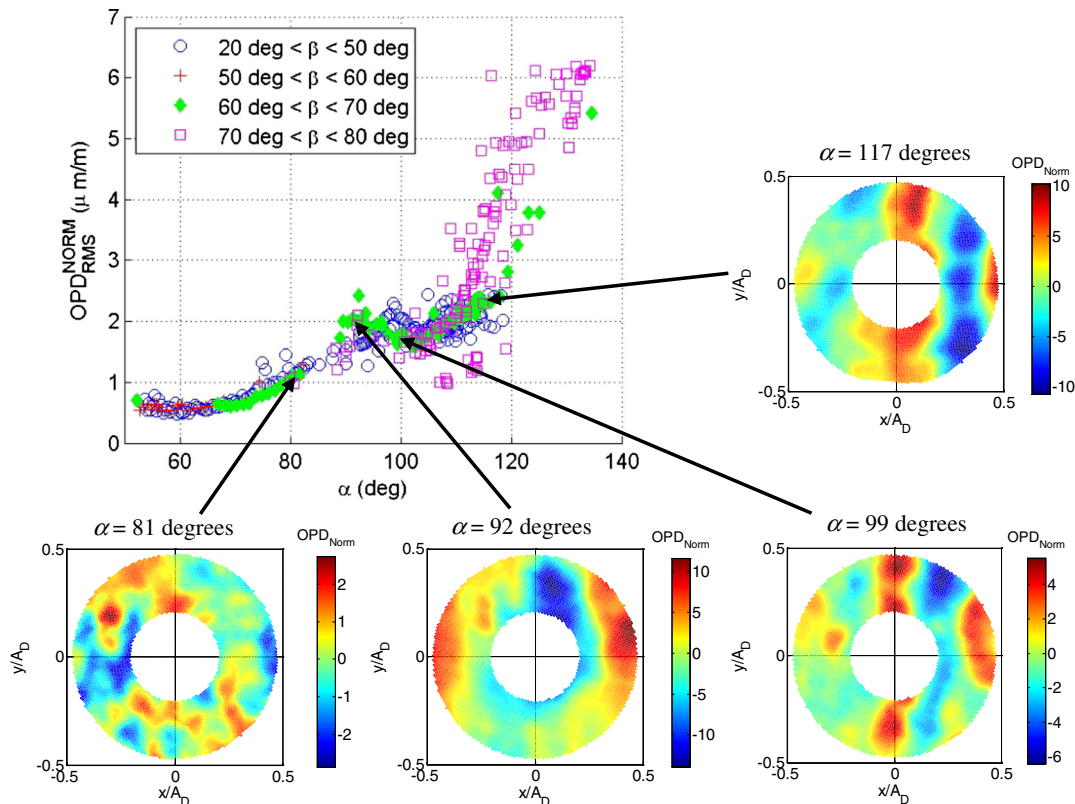


Fig. 2 Normalized OPD_{RMS} for the data for a range of viewing and modified elevation angles with the representative instantaneous realizations of wavefronts across the aperture of the turret at selected angles of $\alpha = 81, 92, 99,$ and 117 deg. The color map in each wavefront is adjusted appropriately to aid in the viewing of the types of aberrations present from structures propagating across the aperture.

In the wavefronts at backward-looking angles, the aberrations appeared as long-spanwise coherent structures resulting from the coherent vortical structures in the shear layer forming over the aperture. Additionally, at the viewing angle of 92 deg, which is near the first peak in the normalized OPD_{RMS} , the upstream portion of the aperture had a local separation bubble that formed from the slope discontinuity of the flat-windowed aperture, causing an increase of aero-optical distortions.¹¹ A detailed analysis of the data and related flow physics is presented in Porter et al.⁹

The data presented in the curve in Fig. 2 were arrived at by calculating the time-averaged normalized spatial OPD_{RMS} across the aperture for different azimuth and elevation angles. From a systems point of view, the primary aero-optic concern is the reduction of the far-field irradiance delivered to the target as a result of these aberrations, typically quantified by the instantaneous and time-averaged Strehl ratios. As mentioned in Sec. 1, if the spatial distribution of the instantaneous wavefront is Gaussian, then the instantaneous OPD_{RMS} can be used in Eq. (2) to predict the instantaneous Strehl ratio accurately¹ without the usual limitation to OPD_{RMS} being less than approximately 0.1λ . For sufficiently large apertures, this assumption was shown to be correct for compressible boundary layers, allowing for the prediction of instantaneous variations of far-field intensity.¹² The question remains whether or not the wavefront data resulting from aero-optic aberrations over the flat-window turret meet this criterion. Figure 3 shows histograms or probability density functions (PDF) of the calculated instantaneous spatial statistics at a viewing angle of 104 deg, using experimentally obtained values from 10,000 consecutive wavefronts frames. In this figure, three histograms are shown corresponding to the normalized OPD_{RMS} [Fig. 3(a)], the skewness γ_1 , [Fig. 3(b)], and the excess γ_2 , [Fig. 3(c)], where the skewness and excess are defined as

$$\gamma_1 = E \left\{ \frac{X - \mu}{\sigma} \right\}^3 = \frac{\mu_3}{\sigma^3}, \quad (5)$$

$$\gamma_2 = E \left\{ \frac{X - \mu}{\sigma} \right\}^4 - 3 = \frac{\mu_4}{\sigma^4} - 3, \quad (6)$$

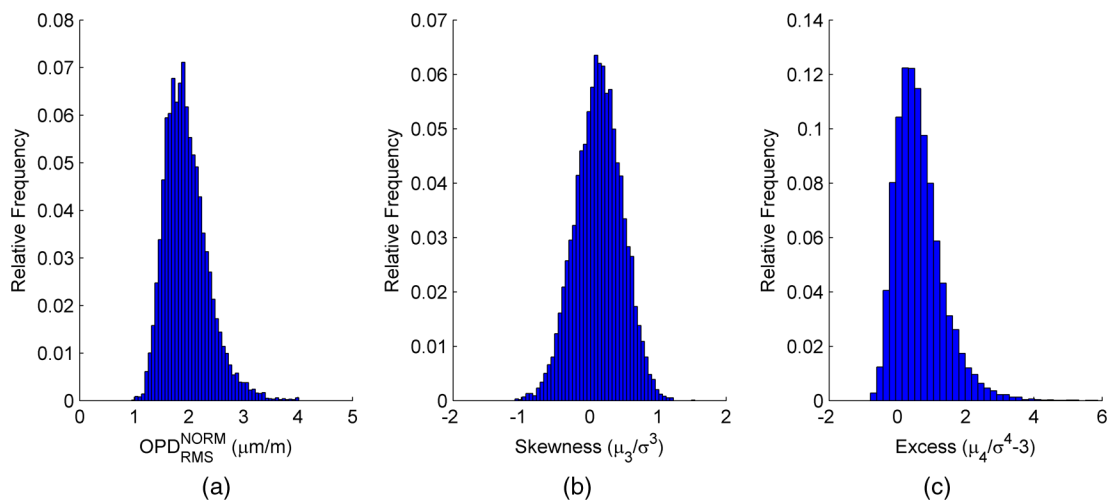


Fig. 3 Histograms of the normalized spatial OPD_{RMS} (a), skewness (b), and excess (c) showing the distribution of values at a viewing angle of $\alpha = 104$ deg.

where X is a random variable (OPD in this case), μ is the wavefront spatial mean (which is zero by definition), μ_3 is the third moment about the mean, μ_4 is the fourth moment about the mean, $\sigma \equiv OPD_{RMS}$ is the wavefront spatial standard deviation, and E is the expectation operator. When the probability distribution function of the instantaneous spatial wavefront is Gaussian, the skewness and excess are exactly zero. As seen in Fig. 3, a large number of the instantaneous wavefronts do not meet the requirement that skewness and excess are zero.

Figure 4 shows the calculated normalized OPD_{RMS} , the skewness, and the excess as a function of the viewing angle for all measured modified elevation angles. The temporal spread of the normalized OPD_{RMS} , skewness, and excess for each data point was defined using the cumulative distribution function CDF from the corresponding experimentally determined PDFs; $CDF(X) = \int_{-\infty}^X PDF(t) dt$. To define the temporal spread, the points where the CDF equaled 0.25 and 0.75 were calculated; these values result in a spread slightly larger than plus or minus one standard deviation from the mean. Error bars on each of the graphs represent the spread in the data. Though the experimental error results in additional scatter in the data, the primary cause of the spread is aero-optic structures convecting across the aperture.

The average skewness and the excess showed a tendency to converge to zero values for $\alpha < 60$ deg, as shown in Fig. 4. This tendency is expected, because at these angles, the aero-optic aberrations result mostly from the turbulent boundary layer present on the forward portion of the turret, and for canonical compressible turbulent boundary layers, instantaneous wavefronts were shown to have Gaussian distribution.¹² Thus, the exponential form of the Maréchal approximation, Eq. (2), is expected to predict the instantaneous Strehl ratio accurately at small forward-looking angles.

As the viewing angle increases past 60 deg, the slope discontinuity from the flat-window aperture causes a local flow separation bubble to form. At this point, the normalized OPD_{RMS} begins to increase as coherent vortical structures form across the aperture, as shown in Fig. 2. Since the wavefront distortion is the result of the presence of coherent vortical structures affected by the intermittent separation bubble,

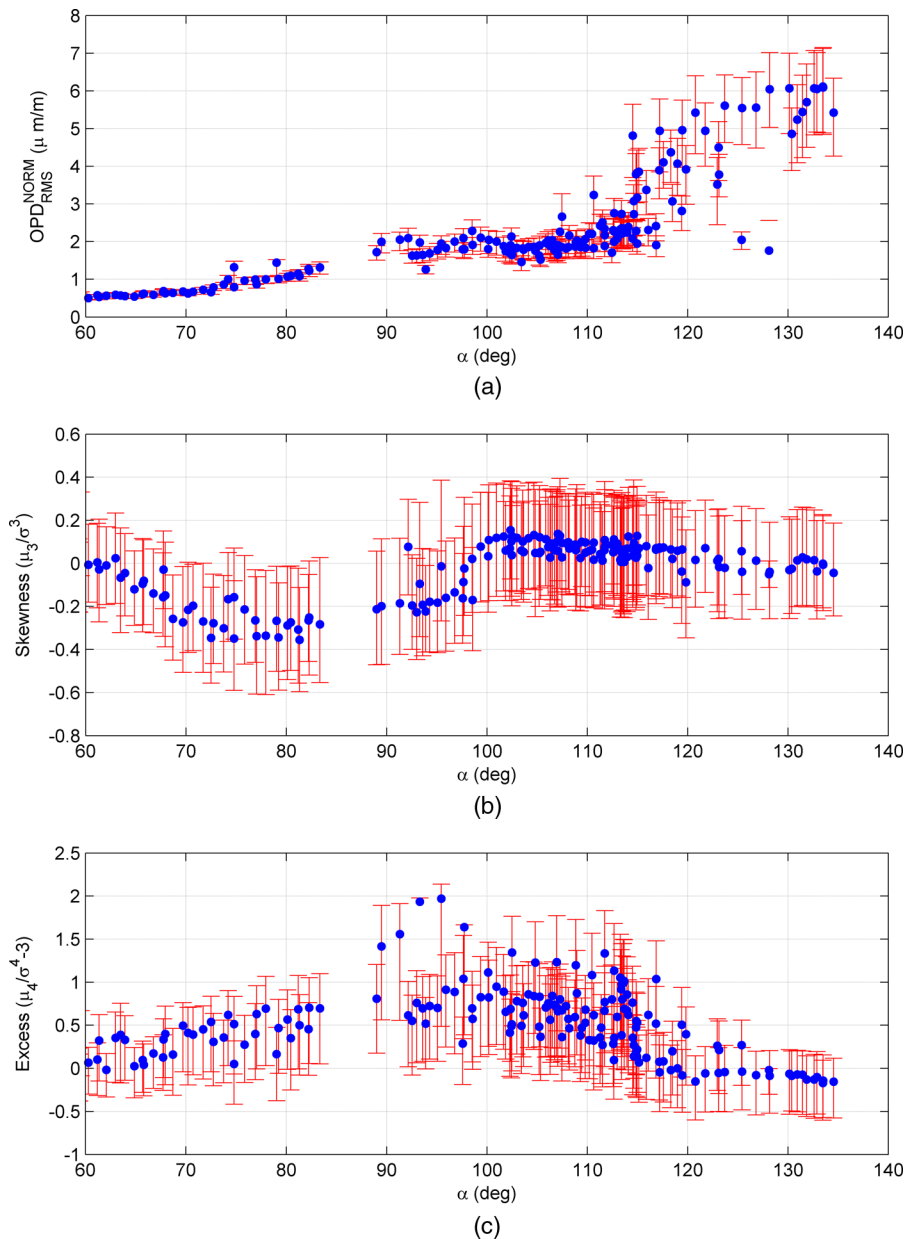


Fig. 4 The normalized OPD_{RMS} (a), skewness (b), and excess (c) over a range of viewing angles. Bars represent 0.25 and 0.75 of the corresponding cumulative distribution function.

the probability distribution function of the OPD across the aperture is no longer Gaussian, and the average skewness values become negative with the corresponding positive excess, as shown in Fig. 4. Finally, as the viewing angle increases past approximately 110 deg, although large coherent structures still can be seen in the wavefronts, the average skewness and excess return to near zero, and the probability distribution function of the OPD is again near Gaussian. However, as shown by the spread, instantaneous values of the skewness and excess deviate from zero as these vortical structures convect across the aperture.

To see how the spatial probability distribution function of the wavefront affects the instantaneous Strehl ratio, an alternative formulation¹ of Eq. (1) yields the instantaneous Strehl ratio for a uniform beam intensity based on the spatial probability distribution function of the OPD:

$$\begin{aligned} SR(t) &= \left| \int_{-\infty}^{\infty} \exp\left(i \frac{2\pi}{\lambda} OPD(x, y, t)\right) PDF(OPD) d(OPD) \right|^2 \\ &= |\phi(2\pi/\lambda)|^2, \end{aligned} \quad (7)$$

where ϕ is the characteristic function or the Fourier transform of the PDF of OPD. For example, the characteristic function of a Gaussian distribution is

$$\phi(2\pi/\lambda) = \exp\left(i\mu(2\pi/\lambda) - \frac{\sigma^2(2\pi/\lambda)^2}{2}\right), \quad (8)$$

where μ is the wavefront mean, which is zero by definition, as the piston mode was removed from each wavefront, and σ is the instantaneous OPD_{RMS} . Substituting Eq. (8) into

Eq. (7) yields the exponential Maréchal approximation, Eq. (2). But for non-Gaussian distributions, the far-field Strehl ratio also depends on the higher-order moments of wavefronts.

To illustrate the effect of non-Gaussian probability distributions, Fig. 5(a) and 5(b) shows the calculated Strehl ratio for time series at a forward-looking angle [$\alpha = 60$ deg, AZ/EL = 47/42 deg; Fig. 5(a) and 5(c)] and a backward-looking angle [$\alpha = 96$ deg, AZ/EL = 110/72 deg; Fig. 5(b) and 5(d)]. From Eq. (1), it follows that the instantaneous Strehl ratio depends on the ratio $\text{OPD}(x, y, t)/\lambda$. Thus, to investigate the temporal variations in Strehl ratios for these viewing angles, we used *the same* experimentally obtained wavefront time series, but instantaneous wavefronts were rescaled using Eq. (4) for different $(\rho/\rho_{\text{SL}})M^2D$, which results in different $\text{OPD}_{\text{RMS}}/\lambda$; physically it means rescaling experimental wavefront results for different turret diameters or altitudes, for instance. The instantaneous Strehl ratios were calculated using rescaled wavefronts and the Fraunhofer approximation, Eq. (1), and they are shown as dots in Fig. 5(a) and 5(b), plotted as a function of the instantaneous rescaled $\text{OPD}_{\text{RMS}}/\lambda$. As discussed before, Eq. (1) is considered the exact solution, as long as assumptions we outlined in Sec. 1 are satisfied. The instantaneous Strehl ratios

significantly vary in time for $\text{OPD}_{\text{RMS}}/\lambda > 0.1$, due to large temporal variations of OPD_{RMS} and other higher-order statistics, as shown in Fig. 4. The time-averaged Strehl ratio, using the Fraunhofer approximation, is shown as a dashed line in Fig. 5(a) and 5(b). This figure also shows the time-averaged Strehl ratio calculated with the large-aperture approximation, Eq. (3), using the time-averaged $\text{OPD}_{\text{RMS}}/\lambda$. At the forward-looking angle shown in Fig. 5(a), the wavefront spatial distribution was nearly Gaussian, and the difference between the time-averaged Strehl ratio and large-aperture approximation is small, although the large-aperture approximation consistently underpredicts time-averaged Strehl ratios. To quantify the difference between approximations, a relative error between the large-aperture approximation and the time-averaged Fraunhofer approximation for the forward-looking angle is presented in the Fig. 5(c). Here the relative error is defined as a modulus of the difference between the Strehl ratio using the large-aperture approximation (LAA) and the time-averaged Fraunhofer approximation, divided by the time-averaged Fraunhofer approximation. Thus,

$$\text{Error} = \left\| \overline{\text{SR}}_{\text{LAA}} - \overline{\text{SR}}_{\text{Fraunhofer}} \right\| / \overline{\text{SR}}_{\text{Fraunhofer}} \quad (9)$$

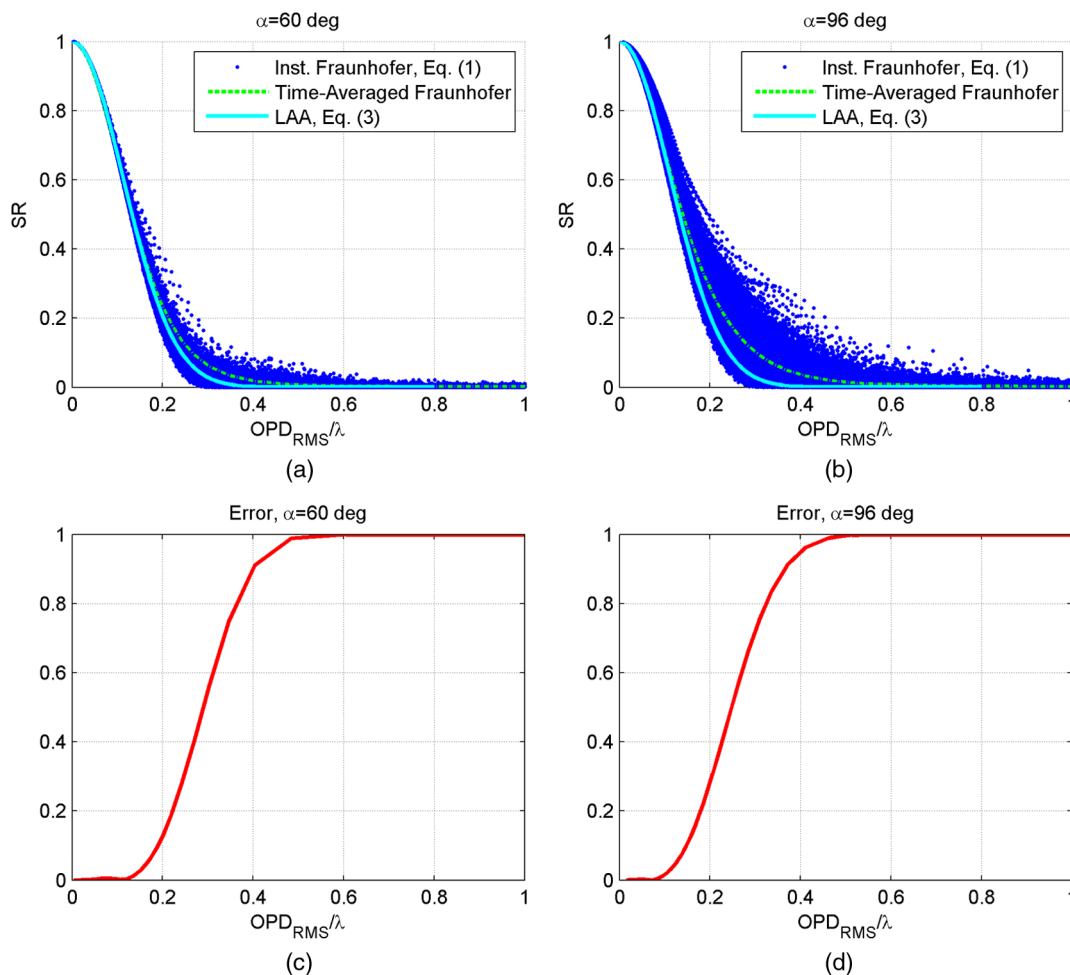


Fig. 5 Comparison of the calculated instantaneous Strehl ratio using the instantaneous wavefronts with the Fraunhofer approximation, Eq. (1), the time-averaged Strehl ratio using the Fraunhofer approximation, and the large-aperture approximation (LAA), Eq. (3), based on the time-averaged $\text{OPD}_{\text{RMS}}/\lambda$ at a viewing angle of $\alpha = 60$ deg (a) and $\alpha = 96$ deg (b). Relative errors between the LAA, Eq. (3) and the time-averaged Fraunhofer approximation for a viewing angle of $\alpha = 60$ deg (c) and $\alpha = 96$ deg (d).

Strehl ratios, computed using the large-aperture approximation, are within 12% from the time-averaged Fraunhofer approximation for OPD_{RMS}/λ less than 0.2, and for larger values of OPD_{RMS}/λ , the relative error quickly approaches 100%. At the backward-looking angle, the difference between the Strehl ratio, computed from experimental data using Eq. (1), and the large-aperture approximation predictions is worse. See the relative error plot in the Fig. 5(d), where the relative error reaches almost 30% at $OPD_{RMS}/\lambda = 0.2$.

The instantaneous Strehl ratios have a lot of scatter about the time-averaged value, which is completely missed when using the large-aperture approximation. A proper analysis of the probability distribution of the OPD_{RMS} should be performed to estimate intensity and relative time percentage of the intensity dropouts,¹² which is important when the turret is used for a free-space, laser-based communication link.

In addition to the Gaussian requirements, the exponential Maréchal approximation, Eq. (2), was originally applied only to instantaneous data.¹ However, it is now common practice to use the large-aperture approximation, Eq. (3), as an approximation for calculating the time-averaged Strehl ratio. But the nonlinear nature of the relation between the instantaneous OPD_{RMS} and the Strehl ratio, Eq. (2), suggests that it should not work for the time average, unless OPD_{RMS}/λ is small, less than 0.1, when the exponent in

Eq. (2) can be expanded in a Taylor series. Rather, the correct way to obtain an estimate of the time-averaged Strehl ratio for a stationary Gaussian process is

$$\overline{SR} = \int \exp[-(2\pi OPD_{RMS}/\lambda)^2] \text{PDF}(OPD_{RMS}) d(OPD_{RMS}), \quad (10)$$

where $\text{PDF}(OPD_{RMS})$ is the probability density function of $OPD_{RMS}(t)$.

Figure 6(a) and 6(b) shows a comparison of the computed time-averaged averaged Fraunhofer approximation, given by Eq. (1), the correct time-averaged Strehl ratio for Gaussian processes, Eq. (10), and the large-aperture approximation, Eq. (3), for two angles. In Fig. 6(a), we see the comparison for the wavefront sequence with a mean excess of 0.38, corresponding to a forward-looking angle, $\alpha = 74$ deg, for $AZ/EL = 66/48$ deg, while the Fig. 6(b) shows results for a larger value of the mean excess of 0.94 for a side-looking angle, $\alpha = 92$ deg, for $AZ/EL = 93/46$ deg. Relative errors, defined by Eq. (9), are given in the Fig. 6(c) and 6(d). When the mean excess is small and the process is approximately Gaussian, the time-averaged Fraunhofer approximation, Eq. (1), and the correct time-averaged Strehl ratio for Gaussian processes, Eq. (10), are within 10% of each other for the given azimuthal/elevation angle for OPD_{RMS}/λ less than

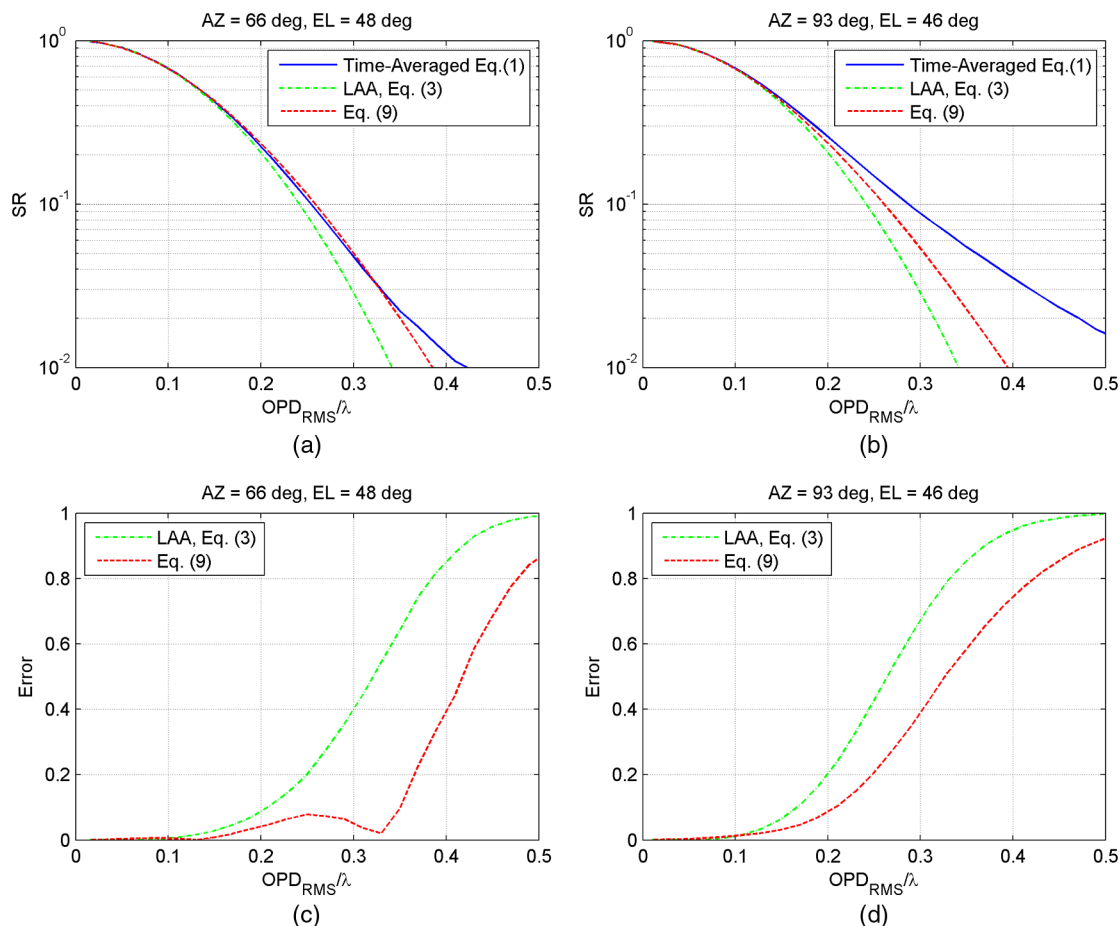


Fig. 6 Time-averaged Strehl ratios using various equations at $AZ = 66$ deg and $EL = 48$ deg (a) and at $AZ = 93$ deg and $EL = 46$ deg (b). Relative errors for the large-aperture approximation, Eq. (3) and Eq. (10), compared to the time-averaged Fraunhofer, Eq. (1), for $AZ = 66$ deg and $EL = 48$ deg (c) and at $AZ = 93$ deg and $EL = 46$ deg (d).

0.35, as shown in the Fig. 6(c). The large-aperture approximation, on the other hand, is more than 60% from the time-averaged Fraunhofer approximation for this value of OPD_{RMS}/λ . When the process is not Gaussian, Fig. 6(d) shows that both Eq. (10) and the large-aperture approximation provide less accurate estimations of the time-averaged Strehl ratio. Still, Eq. (10) provides a slightly better estimate of the time-averaged Strehl ratio, within 10% up to $OPD_{RMS}/\lambda = 0.2$, while the large-aperture approximation is only within 20% at $OPD_{RMS}/\lambda = 0.2$. For larger OPD_{RMS}/λ , both approximations provide progressively less accurate estimations of the Strehl ratio.

As shown in Fig. 4(a), the instantaneous Strehl ratio significantly fluctuates about the mean value. To illustrate this phenomenon, let us consider, for simplicity, a one-dimensional sinusoidal wavefront with a constant wavelength Λ convecting over the aperture Ap at a constant speed U_C , where

$$W(x, t) = \sin\left(\frac{2\pi}{\Lambda}[x - U_C t]\right).$$

Here Λ can be treated as the aero-optical structure size. After removing the instantaneous tilt and piston modes from the instantaneous wavefront inside the aperture, instantaneous $OPD_{RMS}(t)$ can be computed for different ratios of Ap/Λ . Results for three different ratios, $Ap/\Lambda = 5, 2, \text{ and } 1$, are presented in Fig. 7. OPD_{RMS} is clearly a function of time, even when several spatial periods are inside the aperture; this instantaneous variation of spatial wavefront statistics will result in the temporal variation of the far-field Strehl ratio. For the in-flight wavefront data, Ap/Λ was estimated⁹ to be between 2 and 3, thus qualitatively explaining a large variation in the instantaneous Strehl ratios, shown in Fig. 5(a) and 5(b).

As it was argued in Gordeyev and Jumper,⁴ for sufficiently large Reynolds numbers, the typical aero-optical structure size is proportional to the turret diameter, and as the diameter-to-aperture ratio is usually between 2 and 3, the aperture-to-structure-size ratio will be largely independent of the Reynolds number. Thus, for hemisphere-on-cylinder turrets like the AAOL turret, instantaneous spatial statistics will be time dependent, with the corresponding large temporal variation in far-field Strehl ratios, regardless of the turret size.

When the ratio between the aperture size and the typical optical-structure size increases, the spatial value of OPD_{RMS} approaches a constant value, independent of time; from Fig. 7, it can be seen that the aperture-to-structure-size ratio should be more than 5 before OPD_{RMS} becomes independent of time. In this case, the probability function for OPD_{RMS} becomes a delta function centered around the constant OPD_{RMS} value. For Gaussian processes, Eq. (10) becomes the large-aperture approximation, Eq. (3); this is the same result obtained by Steinmetz.⁸ One should note that, as mentioned before, this aperture-to-structure-size ratio is not reached for realistic, AAOL-like turrets, so the large-aperture approximation, Eq. (3), is still only an approximation when applied to aero-optical distortions around turrets at subsonic speeds.

In a case when a stationary structure is present over the aperture (an unsteady defocus, for instance), OPD_{RMS} is

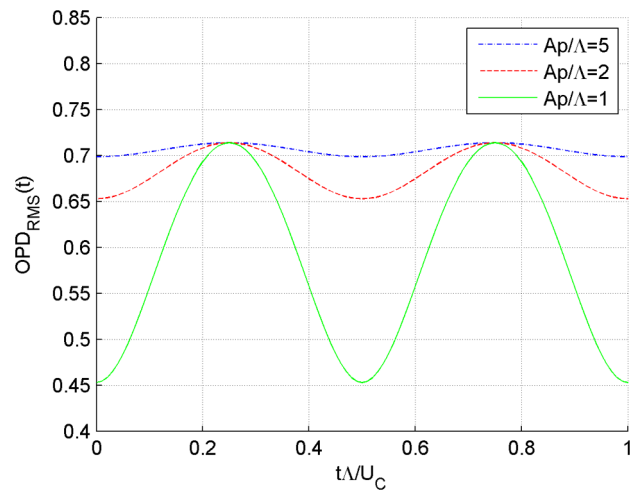


Fig. 7 Instantaneous $OPD_{RMS}(t)$ for a pure convecting one-dimensional wavefront, $W(x, t) = \sin(\frac{2\pi}{\Lambda}[x - U_C t])$, for different apertures.

always a function of time, regardless of the aperture size. Again, the large-aperture approximation, Eq. (3), provides only an approximation of the time-averaged Strehl ratio. For Gaussian processes, Eq. (10) gives an exact answer.

Although it was shown that the large-aperture approximation consistently underpredicts the time-averaged Strehl ratio, for the data analyzed, it still gives a simple way to compute an approximate value for the Strehl ratio for relatively small values of OPD_{RMS} less than 0.2. A partial reason for that is that the spatial distribution for analyzed wavefronts was still almost Gaussian, because the skewness and the excess were relatively small. In the case of wavefronts with a spatial probability very different from the Gaussian distribution, caused by the tip vortices from a helicopter blade,¹³ for example, the large-aperture approximation was shown to predict the time-averaged values of the far-field intensity inaccurately.

3 Conclusions

The large-aperture approximation, Eq. (3), is commonly used to predict system implications of aberrated wavefronts due to whatever cause, with the caveat of its limitation to OPD_{RMS}/λ being restricted to values less than 0.1. As has been discussed here, this restriction is often exceeded for aero-optical aberrations for lasers propagated from turrets on airborne platforms. Because of its common use, this paper has examined the use of the large-aperture approximation for wavefronts collected in flight on the AAOL. The temporally and spatially resolved wavefronts for these in-flight data propagating from the flat-window turret over a range of azimuth and elevation angles at flight Mach number of 0.5 were analyzed. In addition to computing the instantaneous spatial OPD_{RMS} values for all measured azimuth and elevation angles, higher-order statistics were calculated and presented.

The use of the large-aperture approximation was shown to yield a reasonable estimation (within 20%) of the actual average Strehl ratio for $OPD_{RMS}/\lambda < 0.2$. It was shown that the large-aperture approximation consistently underpredicts the time-averaged intensity on a target. In this sense, the Strehl ratio predicted by Eq. (3) could be considered a conservative

or worst-case estimate of the Strehl ratio, at least for almost Gaussian processes. A better prediction of the time-averaged Strehl ratio is possible by using a “corrected” form of the large-aperture equation based on the probability distribution and given in Eq. (10). Using Eq. (10), for moderate levels of aero-optical distortions, $OPD_{RMS}/\lambda < 0.3$, the agreement was shown to be within 20% when the spatial probability distribution of wavefronts was Gaussian and within 40% when the distribution deviated from Gaussian. For the same range of aero-optical distortions, the large-aperture approximation was only within 60%, or less than a half of the time-averaged Fraunhofer Strehl ratio.

In addition, the higher-order statistics were found to be of value in identifying regions over the turret where some unique flow physics might be occurring. At the viewing-angle range between 70 and 100 deg, for example, we were able to associate the non-Gaussian behavior with the presence of a separation bubble at the leading edge of the flat window.

Finally, large instantaneous variations of the Strehl ratio around the time-averaged value were observed for all viewing angles and qualitatively explained. These far-field intensity variations can lead to a series of short intensity dropouts on the target, potentially hurting the performance for free-space laser communications. Thus, these dropouts should be taken into consideration when analyzing and/or designing beam-control systems to mitigate aero-optical effects.

Acknowledgments

The authors would like to thank the Northern Air personnel, especially Kevin Tessmer, for providing technical assistance during our flight test. We would also like to thank Matthew Krizo from AFIT for providing assistance on the laser tracking system. These efforts were sponsored by the

High Energy Laser Division of the Joint Technology Office (HEL JTO) and supported by the Air Force Office of Scientific Research, Grant No. FA9550-07-1-0574. The U.S. government is authorized to reproduce and distribute reprints for governmental purposes notwithstanding any copyright notation thereon.

References

1. T. S. Ross, “Limitations and applicability of the Maréchal approximation,” *Appl. Opt.* **48**(10), 1812–1818 (2009).
2. R. Butts and L. D. Weaver, “Airborne laser experiment (ABLEX): theory and simulations,” *Proc. SPIE* **2120**, 10 (1994).
3. L. D. Weaver and R. Butts, “ABLEX: high altitude laser propagation experiment,” *Proc. SPIE* **2120**, 30 (1994).
4. S. Gordeyev and E. J. Jumper, “Fluid dynamics and aero-optics of turrets,” *Prog. Aerospace Sci.* **46**(8), 388–400 (2010).
5. M. Wang, A. Mani, and S. Gordeyev, “Physics and computation of aero-optics,” *Ann. Rev. Fluid Mech.* **44**(1), 299–321 (2012).
6. E. Jumper et al., “Airborne aero-optics laboratory,” *Opt. Eng.* **52**(7), 071408 (2013).
7. M. Born and E. Wolf, *Principles of Optics*, 7th ed., Cambridge University Press, Cambridge (1999).
8. W. J. Steinmetz, “Second moments of optical degradation due to a thin turbulent layer,” in *Aero-Optical Phenomena*, *Progress in Astronautics and Aeronautics*, K. G. Gilbert and L. J. Otten, Eds., Vol. 80, pp. 78–110, AIAA, New-York (1982).
9. C. Porter et al., “Flight measurements of the aero-optical environment around a flat-windowed turret,” to appear in *AIAA J.* (2013).
10. N. De Lucca, S. Gordeyev, and E. Jumper, “In-flight aero-optics of turrets,” *Opt. Eng.* **52**(7), 071405 (2013).
11. S. Gordeyev et al., “Aero-optical environment around a cylindrical turret with a flat window,” *AIAA J.* **49**(2), 308–315 (2011).
12. S. Gordeyev, J. Cress, and E. Jumper, “Far-field laser intensity drop-outs caused by turbulent boundary layers,” to appear in *J. Directed Energy* (2013).
13. C. Porter, “The optical environment from the tip vortices of a helicopter in different flight regimes,” Ph.D. Thesis, University of Notre Dame (2011).

Biographies and photographs of the authors are not available.